



# Mechanism insight into rapid photocatalytic disinfection of *Salmonella* based on vanadate QDs-interspersed g-C<sub>3</sub>N<sub>4</sub> heterostructures

Rong Wang<sup>a</sup>, Xiangyu Kong<sup>a</sup>, Wentao Zhang<sup>a</sup>, Wenxin Zhu<sup>a</sup>, Lunjie Huang<sup>a</sup>, Jing Wang<sup>a</sup>, Xu Zhang<sup>a</sup>, Xinnan Liu<sup>a</sup>, Na Hu<sup>b</sup>, Yourui Suo<sup>b</sup>, Jianlong Wang<sup>a,\*</sup>

<sup>a</sup> College of Food Science and Engineering, Northwest A&F University, Yangling 712100, Shaanxi, China

<sup>b</sup> Qinghai Key Laboratory of Qinghai-Tibet Plateau Biological Resources, Northwest Institute of Plateau Biology, Chinese Academy of Sciences, Qinghai, 810008, China

## ARTICLE INFO

### Keywords:

Vanadate QDs

g-C<sub>3</sub>N<sub>4</sub>

Photocatalytic disinfection

Leakage of cell contents

## ABSTRACT

Photocatalytic disinfection, which is a readily reliable method in most climates, holds great promise to significantly reduce the microbial contamination in modern industry. Here we report that vanadate quantum dots-interspersed graphitic carbon nitride (vanadate QDs/g-C<sub>3</sub>N<sub>4</sub>) can achieve efficient inactivation of *Salmonella* by harvesting a substantial visible light. Detailed characterization through SEM-EDS, TEM, XRD, FT-IR, and XPS confirmed the formation of the composites. Owing to the efficient reactive oxygen species (ROS) production between vanadate QDs and g-C<sub>3</sub>N<sub>4</sub>, the bactericidal efficiency of AgVO<sub>3</sub> QDs/g-C<sub>3</sub>N<sub>4</sub> could reach 96.4% toward *Salmonella* in a concentration of 0.75 mg/mL after 10 min visible-light illumination. More importantly, scavenger experiments of different reactive species proved that the photoinduced electron generated at the oxidation site of AgVO<sub>3</sub>/g-C<sub>3</sub>N<sub>4</sub> play a major role as oxidative species. Fluorescent-based cell live/dead test and membrane potentials were applied to demonstrate the integrity of cell membranes. Furthermore, the SEM technology, PCR and BCA protein assay were employed to verify the bacterial decomposition as well as leakage of bacterial cell contents toward *Salmonella*. Sterilization experiments of *Staphylococcus aureus* revealed that our composites have broad spectrum antimicrobial activity for both Gram-negative and Gram-positive bacteria under visible light. The results showed that the generation of high ROS could attack the bacterial cells membrane, and ultimately disrupt the cell metabolism through bacterial contents, which provided a feasible method for eliminating the microbial contaminated water.

## 1. Introduction

Microbial contamination has always been a threat to human health all over the world, and millions of deaths are caused by pathogenic microorganisms every year [1–3]. Therefore, enormous efforts have been focused on exploring efficient disinfection methods, including chemical disinfection using chlorine microbe degradation, UV irradiation and photocatalytic disinfection [4–8]. Among these methods, photocatalytic disinfection, which may replace the conventional chemical process, hold great promise for the remediation of microbial contamination as it can avoid some disadvantages, such as energy consumption, low efficiency and generation of carcinogenic byproducts [9–11]. Taking this into account, photocatalytic disinfection has attracted more and more interest from the perspective of energy consumption as well as hypotoxicity, and seeking a novel photocatalyst that can harvest the whole spectrum visible light for rapid photocatalytic disinfection is absolutely vital [12,13].

Recently, graphitic carbon nitride (g-C<sub>3</sub>N<sub>4</sub>), a metal-free polymeric semiconductor with a narrow bandgap of  $\approx 2.7$  eV, has elicited ripples of excitement in the field of next-generation photocatalyst research as it can harvest a substantial visible light for achieving highly efficient photocatalytic performance [14–16]. The unique properties of g-C<sub>3</sub>N<sub>4</sub> nanosheets, including large surface area, excellent chemical stability and tunable electron band structure, have expanded its applications particularly as a feasible alternative for TiO<sub>2</sub>-based photocatalysts in removal of microbial contamination. Importantly, g-C<sub>3</sub>N<sub>4</sub> is readily prepared by thermal polymerization of “earth-abundant” nitrogen-rich precursors such as dicyandiamide [17–19], urea [20–22], thiourea [23] and melamine [24]. Among these precursors, urea has been recently found to be an excellent precursor for synthesizing sheet-like g-C<sub>3</sub>N<sub>4</sub> with high specific surface area and high porosity [25,26]. However, there is an inherent drawback for urea-derived-g-C<sub>3</sub>N<sub>4</sub>, in which the production of electron-hole pairs could be rapidly recombined during visible light irradiation. This issue makes urea-derived-g-C<sub>3</sub>N<sub>4</sub> a low

\* Corresponding author.

E-mail address: [wanglong79@yahoo.com](mailto:wanglong79@yahoo.com) (J. Wang).

<https://doi.org/10.1016/j.apcatb.2017.11.060>

Received 7 September 2017; Received in revised form 9 November 2017; Accepted 24 November 2017

Available online 02 December 2017

0926-3373/ © 2017 Elsevier B.V. All rights reserved.

conversion efficiency of solar energy and greatly obstructs its practical application. Thereupon, a great deal of effort has been devoted to endow g-C<sub>3</sub>N<sub>4</sub>, such as forming heterostructures [27,28], doping with metals [29–31], and synthesizing hollow nanospheres [32], etc. Among these photocatalysts developed to date, heterostructures, especially vanadate QDs-interspersed g-C<sub>3</sub>N<sub>4</sub> heterostructures have attracted significant attention due to their superior interfacial charge transfer, for which could overcome the rapid recombination of photogenerated electron-hole pairs of g-C<sub>3</sub>N<sub>4</sub> and thus enhancing the photocatalytic disinfection [33].

Vanadate QDs, as one of the 0-dimensional (0D) semiconductive QDs, have attracted a dramatic interest due to their exceptional advantages of small size, tunable optical absorptivity, and excellent electron transfer rates, which make them remarkably promising in the field of photocatalysts for solar light harvesting [34–36]. Despite these unique advantages, the use of vanadate quantum dots as photocatalysts is limited in two aspects. First, vanadate quantum dots are easily self-aggregated and the surface defects make themselves unstable in comparison with other bulk semiconductors. Second, the high photoluminescence of quantum dots could lead to the recombination of electron-hole pairs [37,38]. One of the most efficient routes to solve these problems is to load QDs onto ultrathin 2-dimensional (2D) nanosheets to form a 2D-nanocomposite [39]. Obviously, urea-derived g-C<sub>3</sub>N<sub>4</sub> is an ideal 2D nanosheets. The synergy effect of establishment of heterostructure between vanadate QDs and g-C<sub>3</sub>N<sub>4</sub> was expected to not only overcome the rapid recombination of photogenerated electron-hole pairs of g-C<sub>3</sub>N<sub>4</sub> but also to reduce the self-aggregation of bare vanadate QDs, and thereby presenting greatly promoted photocatalytic disinfection [40].

Herein, we constructed vanadate (AgVO<sub>3</sub>, BiVO<sub>4</sub>) QDs/g-C<sub>3</sub>N<sub>4</sub> utilizing urea as precursor and demonstrated their outstanding photocatalytic disinfection toward *Salmonella* H9812 for the first time, significantly better than those of single g-C<sub>3</sub>N<sub>4</sub> and most of g-C<sub>3</sub>N<sub>4</sub>-based composite photocatalysts reported to date. The photocatalytic disinfection effects of vanadate QDs/g-C<sub>3</sub>N<sub>4</sub> toward *Salmonella* were systematically studied by a plate count approach under visible light irradiation. Scavenger experiments were employed to investigate the major reactive oxidative species in photocatalytic disinfection process. In addition, the lethal effects and cell destruction on bacteria, which caused by vanadate QDs/g-C<sub>3</sub>N<sub>4</sub> composites under visible light irradiation, were investigated by fluorescent-based cell live/dead tests, membrane potential, SEM observation of bacteria, and detection of leakage in bacterial contents. The excellent properties associated with vanadate QDs-interspersed g-C<sub>3</sub>N<sub>4</sub> heterostructures indicate that they can be used as a novel and effective light harvesting catalysts for photocatalytic disinfection.

## 2. Experimental section

### 2.1. Materials

Silver nitrate (AgNO<sub>3</sub>) were purchased from kermel Chemical Reagent Co., Ltd (Tianjin China), sodium oxalate, ammonium metavanadate and fluorescein isothiocyanate (FITC) were purchased from Aladdin chemistry Co. Ltd. (Shanghai, China), 2,2,6,6-Tetramethylpiperidine (TEMPOL) and ethylenediaminetetraacetic acid disodium salt (Na<sub>2</sub>EDTA) was purchased from Sigma-Aldrich (St. Louis, MO), ammonium hydroxide, isopropanol and anhydrous ethanol (EtOH, AR) were purchased from Kelong Chemical Reagent Co., Ltd. (Chengdu, China), urea was purchased from Beijing Solarbio Science & Technology Co., Ltd (Beijing, China), bismuth nitrate was purchased from Xiya Chemical Reagent Co., Ltd (Shandong China), DiBAC<sub>4</sub>(3) was purchased from ATT Bioquest (Sunnyvale, USA), propidium iodide (PI) was purchased from MP Biomedicals Co., Ltd (Shanghai, China). BCA Protein Assay Kit was obtained from Heart Zbiological Technology Co., Ltd (Xi'an, China). The water used in all experiments was de-ionized

(DI). All of the chemical reagents of analytical grade were used as received without further purification.

### 2.2. Synthesis of the g-C<sub>3</sub>N<sub>4</sub>

Urea was put in a covered crucible, heated over 4 h to 550 °C in air and kept at this temperature for another 4 h. The as-formed yellow solid was the g-C<sub>3</sub>N<sub>4</sub>.

### 2.3. Synthesis of the vanadate QDs/g-C<sub>3</sub>N<sub>4</sub>

Vanadate QDs/g-C<sub>3</sub>N<sub>4</sub> was prepared by an ultrasonic reaction route. Firstly, 0.482 g-C<sub>3</sub>N<sub>4</sub> was initially added into 30 mL AgNO<sub>3</sub> aqueous solution with a concentration of 5 mmol/L to prepare a uniform suspension. After vigorous stirring for 30 min, 30 mL NH<sub>4</sub>VO<sub>3</sub> solution (5 mmol/L) were added into the mixed solution, followed by another 30 min stirring. The pH of the solutions was adjusted to 7 with ammonium hydroxide. Then the solutions were ultrasonic for 60 min until vanadate crystallized. The obtained precipitates were separated by centrifugation, and washed with deionized water and anhydrous ethanol to remove the organics. Finally, the product was dried at 80 °C in vacuum oven for 24 h for further use and characterization. BiVO<sub>4</sub>/g-C<sub>3</sub>N<sub>4</sub> were synthesized in the same way. The ICP-MS results showed that the weight ratio of AgVO<sub>3</sub> QDs in AgVO<sub>3</sub>/g-C<sub>3</sub>N<sub>4</sub> was 24.1%, and the weight ratio of BiVO<sub>4</sub> QDs in the composites of BiVO<sub>4</sub>/g-C<sub>3</sub>N<sub>4</sub> was 22.6%.

### 2.4. Characterization

The X-ray diffraction (XRD) patterns of the crystal phase were using a Bruker D8 diffractometer with high-intensity Cu-Kα in the 2θ range of 10–70°. Fourier-transform infrared (FTIR) spectra were carried out using a Vetex70 (Bruker Corp, Germany). Scanning electron microscopy (SEM) image and energy dispersive spectroscopy (EDS) analysis were performed by S-4800 FE-SEM (Hitachi, Japan). High-resolution transmission electron microscopy (HRTEM) images were taken on a FEI Electron optics GZF2.0 electron microscope at an acceleration voltage of 200 kV. X-ray photoelectron spectroscopy (XPS) data was collected using an Axis Ultra DLD X-ray photoelectron spectrometer equipped with an Al-Kα X-ray source (1486.6 eV). UV–vis diffuse reflectance absorbance spectra of all composites were recorded by using a UV–vis spectrophotometer (UV-3600, Shimadzu, Japan). The photoluminescence (PL) spectra of composites were recorded by F-7000 fluorescence spectrophotometer (Hitachi, Japan). Membrane potential for fluorescence was measured at the excitation and emission wavelengths of 485 and 535 nm, using a fluorescence microplate reader (PE, VictorX3, USA). The fluorescent-based cell live/dead tests were recorded with a fluorescence microscope (Olympus IX71, Tokyo, Japan). The amount (weight ratio%) of the AgVO<sub>3</sub>, BiVO<sub>4</sub> QDs in the composites were quantified by ICP-MS (ICAP Qc, Thermo Scientific, USA). All pH measurements were performed with a PB-10 digital pH-meter (Sartorius, Germany) with a combined glass-calomel electrode.

### 2.5. Photocatalytic disinfection tests

*Salmonella* H9812 was purchased from BeNa Culture Collection, and it is a kind of pathogenic bacterium that called *Salmonella* Braenderup. The photocatalytic disinfection abilities of g-C<sub>3</sub>N<sub>4</sub>, AgVO<sub>4</sub>/g-C<sub>3</sub>N<sub>4</sub>, BiVO<sub>4</sub>/g-C<sub>3</sub>N<sub>4</sub> were evaluated via the inactivation of *Salmonella* Braenderup H9812 under visible light irradiation. Before the microbiological experiments, all of the glasswares and the culture medium solution were sterilized by autoclaving at 121 °C for 30 min. And all the experiments were processed under sterile conditions. The bacterial cells were cultured in nutrient solution at 37 °C for 18 h and centrifuged to remove the metabolites, then diluted with phosphate buffer solution (PBS, 0.01 M, pH 7.4) to yield a cell count of approximately 10<sup>7</sup> colony-

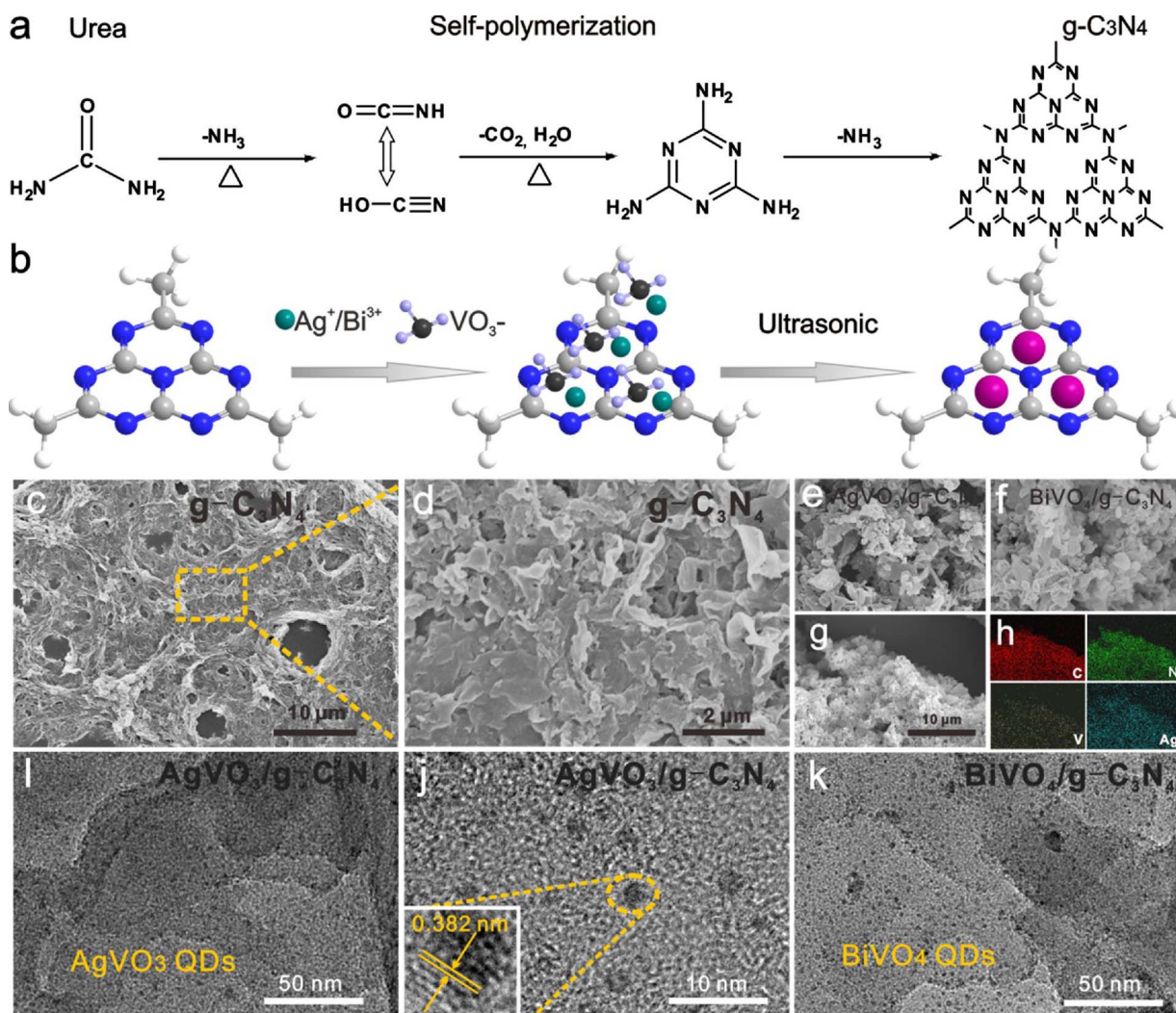


**Fig. 1.** (a) The self-polymerization of urea into a graphitic carbon nitride network at high temperatures. (b) Formation mechanism of vanadate QDs/g-C<sub>3</sub>N<sub>4</sub>. (c) SEM image of urea-derived g-C<sub>3</sub>N<sub>4</sub>. (d) Magnified SEM image of urea-derived g-C<sub>3</sub>N<sub>4</sub>. (e) SEM image of AgVO<sub>3</sub>/g-C<sub>3</sub>N<sub>4</sub>. (f) SEM image of BiVO<sub>4</sub>/g-C<sub>3</sub>N<sub>4</sub>. (g) SEM image of AgVO<sub>3</sub>/g-C<sub>3</sub>N<sub>4</sub> for EDS. (h) The corresponding elemental mappings of C, N, Ag and V elements in Fig. 1g. (i) HRTEM image of AgVO<sub>3</sub>/g-C<sub>3</sub>N<sub>4</sub>. (j) HRTEM image of AgVO<sub>3</sub>/g-C<sub>3</sub>N<sub>4</sub>. (k) HRTEM image of BiVO<sub>4</sub>/g-C<sub>3</sub>N<sub>4</sub>.

forming units per milliliter (CFU/mL). For each antibacterial experiment, 20 mL of *Salmonella* suspension and 15 mg catalyst powders were pipetted into a container. Then, the antibacterial experiment was initiated by irradiating the suspension with a commercial 300 W xenon lamp (Perfectlight Technology, Beijing) equipped with a UV cut off filter ( $\lambda > 400$  nm) under illumination of AM 1.5 G. The light source was located 20 cm from the reaction solution (100 mW cm<sup>-2</sup> illumination intensity). At given irradiation time interval (0, 5, 10, 20, 30 min), 100  $\mu$ L of tested suspension samples were spread on freshly prepared LB agar plates, and the colonies were counted to determine the survival bacterial numbers after incubation at 37 °C for 24 h. Experiments on different concentration of photocatalysts were also perform by this method. At the same time, light control experiments (*Salmonella* without photocatalyst under illumination) and dark control experiments (*Salmonella* with photocatalyst in dark) were also performed. The bacterial inactivation efficiencies of g-C<sub>3</sub>N<sub>4</sub>, AgVO<sub>4</sub>/g-C<sub>3</sub>N<sub>4</sub>, and BiVO<sub>4</sub>/g-C<sub>3</sub>N<sub>4</sub> were calculated using by the equation (Eq. (1)):

$$\text{Bactericidal efficiency (\%)} = \frac{N_0 - N_t}{N_0} \times 100\% \quad (1)$$

Where  $N_0$  and  $N_t$  corresponding to the numbers of colonies counted in the control and sample of culture medium plates, respectively [41].

### 3. Results and discussions

#### 3.1. Morphology and crystal structure characterization

Fig. 1a presented the possible microscopic mechanism of urea conversion into the g-C<sub>3</sub>N<sub>4</sub> nanosheets at high temperature. During the thermal treatment process, the oxygenated compounds act as additional leaving motifs to promote condensation of carbonitride materials, and resulting in self-polymerizing g-C<sub>3</sub>N<sub>4</sub> [25,26]. Fig. 1b presented the formation mechanism of vanadate QDs/g-C<sub>3</sub>N<sub>4</sub> nanosheets. The g-C<sub>3</sub>N<sub>4</sub> nanosheets could capture metal cations into their tri-triazine units through nitrogen complexes, which results in the formation of stable and highly dispersed vanadate QDs. Followed by sonication, the vanadate QDs interspersed g-C<sub>3</sub>N<sub>4</sub> heterostructures were formed. To verify the morphology and superficial microstructure of vanadate QDs/g-C<sub>3</sub>N<sub>4</sub> materials, scanning electron microscopy (SEM) and high-resolution transmission electron microscopy (HRTEM) were investigated. The SEM image of urea-derived g-C<sub>3</sub>N<sub>4</sub> in Fig. 1c displayed a two-dimensional structure consisting of small flat sheets with wrinkle. Fig. 1d recorded at high magnification clearly show the porous g-C<sub>3</sub>N<sub>4</sub> photocatalyst with chiffon-like ripples and wrinkles. As shown on Fig. 1e–f, after the materials were fabricated, the morphology of AgVO<sub>3</sub>/g-C<sub>3</sub>N<sub>4</sub> and BiVO<sub>4</sub>/g-C<sub>3</sub>N<sub>4</sub> does not change much, well inherited the sheet-like morphology from their g-C<sub>3</sub>N<sub>4</sub> precursor. Fig. 1g–h were a

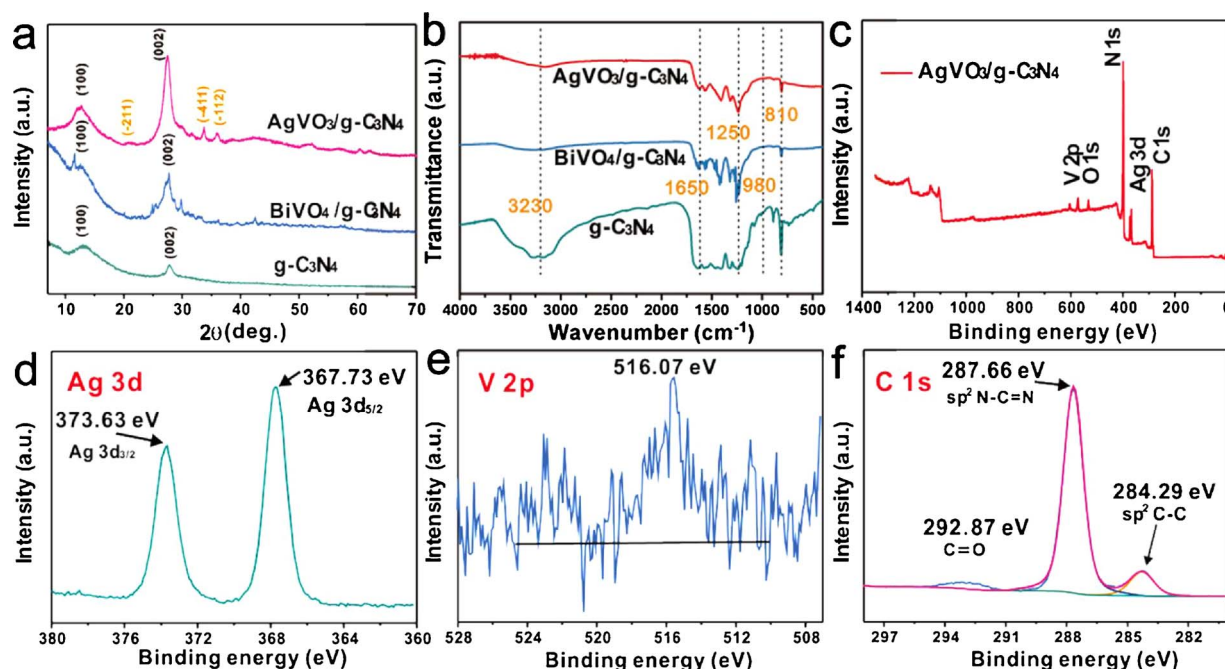


Fig. 2. (a) XRD patterns of g-C<sub>3</sub>N<sub>4</sub>, AgVO<sub>3</sub>/g-C<sub>3</sub>N<sub>4</sub> and BiVO<sub>4</sub>/g-C<sub>3</sub>N<sub>4</sub>. (b) IR spectra of g-C<sub>3</sub>N<sub>4</sub>, AgVO<sub>3</sub>/g-C<sub>3</sub>N<sub>4</sub> and BiVO<sub>4</sub>/g-C<sub>3</sub>N<sub>4</sub>. (c) XPS spectra of AgVO<sub>3</sub>/g-C<sub>3</sub>N<sub>4</sub>. (d) High-resolution Ag 3d XPS spectra of AgVO<sub>3</sub>/g-C<sub>3</sub>N<sub>4</sub>. (e) High-resolution V 2p XPS spectra of AgVO<sub>3</sub>/g-C<sub>3</sub>N<sub>4</sub>. (f) High-resolution C 1s XPS spectra of AgVO<sub>3</sub>/g-C<sub>3</sub>N<sub>4</sub>.

representative images of AgVO<sub>3</sub>/g-C<sub>3</sub>N<sub>4</sub> with energy-dispersive X-ray spectroscopy (EDS) elemental mapping for C, N, Ag and V. In the elemental map, the brighter area indicated a higher concentration of the corresponding element. Obviously, the mapping clearly revealed that Ag element and V element are highly dispersed in the composites, which confirms that our composites were successfully synthesized. Moreover, we have performed HRTEM analysis on vanadate QDs/g-C<sub>3</sub>N<sub>4</sub> to observe vanadate QDs (Fig. 1i–k). It can be seen that many particles with diameters < 5 nm are decorated on the surface of g-C<sub>3</sub>N<sub>4</sub> nanosheets in comparison with bare g-C<sub>3</sub>N<sub>4</sub> (Fig. S1). As presented in Fig. 1i, the surface of g-C<sub>3</sub>N<sub>4</sub> becomes rough after coupling with AgVO<sub>3</sub> QDs, manifesting a substantial loading of objective substances. A typical lattice distance of 0.382 nm identified that AgVO<sub>3</sub> were highly crystalline (Fig. 1j). For BiVO<sub>4</sub>/g-C<sub>3</sub>N<sub>4</sub> nanosheets, the panoramic view shown in Fig. 1k reveals that g-C<sub>3</sub>N<sub>4</sub> nanosheets are highly dispersed of BiVO<sub>4</sub> QDs, and the lattice of BiVO<sub>4</sub> QDs can be clearly seen in Fig. S2. All of the results indicated that our composites were successfully synthesized. With the loaded vanadate QDs, porous g-C<sub>3</sub>N<sub>4</sub> photocatalyst may significantly improve its ability of charge separation, favoring enhanced photocatalysis.

The XRD patterns of AgVO<sub>3</sub>/g-C<sub>3</sub>N<sub>4</sub>, BiVO<sub>4</sub>/g-C<sub>3</sub>N<sub>4</sub> and g-C<sub>3</sub>N<sub>4</sub> were presented in Fig. 2a. For g-C<sub>3</sub>N<sub>4</sub> (curve green), the strong shoulder peak is found at 2θ of 27.84°, originating from the (002) inter-planar stacking peak of conjugated aromatic systems. Another distinct peak (100) at around 13.1° can be attributed to an in-planar structural packing motif [25]. While for AgVO<sub>3</sub>/g-C<sub>3</sub>N<sub>4</sub> (curve red), it exhibits an apparent peak at 27.53°, which was attributed to (002) diffraction of the g-C<sub>3</sub>N<sub>4</sub>. In addition, no sharpening diffraction peaks of AgVO<sub>3</sub> QDs were observed in AgVO<sub>3</sub>/g-C<sub>3</sub>N<sub>4</sub>, revealing the small size of vanadate QDs maintained by our in situ growth strategy. For BiVO<sub>4</sub>/g-C<sub>3</sub>N<sub>4</sub> (curve blue), the strongest peak was found at 2θ of 27.77°, originating from the (002) inter-planar stacking peak. Besides, some of the small peaks in the XRD pattern at 2θ of 20° and 50° can be attributed to the presence of BiVO<sub>4</sub> QDs with very low content [33]. The fourier transform infrared spectroscopy (FT-IR) of AgVO<sub>3</sub>/g-C<sub>3</sub>N<sub>4</sub>, BiVO<sub>4</sub>/g-C<sub>3</sub>N<sub>4</sub> and g-C<sub>3</sub>N<sub>4</sub> were presented in Fig. 2b. In the spectrum of g-C<sub>3</sub>N<sub>4</sub>, the serial bands between 1650 and 1250 cm<sup>-1</sup> can be ascribed to the existence of CN heterocycles. The broad absorption band at about 3230 cm<sup>-1</sup> is due to

the N–H stretching vibration modes of g-C<sub>3</sub>N<sub>4</sub>. The sharp peak at 810 cm<sup>-1</sup> is ascribed to the stretching vibration modes of tri-triazine units, which is the main motif of the g-C<sub>3</sub>N<sub>4</sub>. For AgVO<sub>3</sub>/g-C<sub>3</sub>N<sub>4</sub> and BiVO<sub>4</sub>/g-C<sub>3</sub>N<sub>4</sub>, very weak band at 980 cm<sup>-1</sup> is ascribed to the VO<sub>3</sub>-groups. The elemental compositions and chemical states of AgVO<sub>3</sub>/g-C<sub>3</sub>N<sub>4</sub>, BiVO<sub>4</sub>/g-C<sub>3</sub>N<sub>4</sub> were further investigated by X-ray photoelectron spectroscopy (XPS) measurement. Fig. 2c displays the survey scan spectra of AgVO<sub>3</sub>/g-C<sub>3</sub>N<sub>4</sub> films. The obvious peaks of Ag, V, C, N and O can be clearly observed in the composites, indicating the successful growth of AgVO<sub>3</sub> QDs on g-C<sub>3</sub>N<sub>4</sub> nanosheets. Fig. 2d shows the high resolution Ag 3d XPS spectrum of AgVO<sub>3</sub>/g-C<sub>3</sub>N<sub>4</sub> nanosheets. For the composites, characteristic peaks at 373.63 eV and 367.73 eV are observed, which are assigned to Ag 3d<sub>3/2</sub> and Ag 3d<sub>5/2</sub>, respectively. Furthermore, the binding energy of 516.07 eV can be assigned to V 2p<sub>3/2</sub> (Fig. 2e). In the high-resolution, C 1s spectra of AgVO<sub>3</sub>/g-C<sub>3</sub>N<sub>4</sub> (Fig. 2f) can be assigned to three peaks, which locating at 292.87, 287.66 and 284.29 eV, respectively. The peak at 292.87 eV can be assigned to C=O bonds between AgVO<sub>3</sub> and g-C<sub>3</sub>N<sub>4</sub>, while the peak at 287.66 eV is corresponding to sp<sup>2</sup> N–C=N bonded. Besides, the peak at 284.29 eV can be ascribed to sp<sup>2</sup> C–C bonds of graphitic carbon. The spectra of BiVO<sub>4</sub>/g-C<sub>3</sub>N<sub>4</sub> were also presented in Fig. S3–S4. It proved that our composites were successfully synthesized. Therefore, based on the analysis of XRD, FT-IR and XPS, the formation of vanadate QDs/g-C<sub>3</sub>N<sub>4</sub> showed a strong interaction between vanadate QDs and g-C<sub>3</sub>N<sub>4</sub> nanosheets, which facilitates their photocatalytic performance by enhancing mass/charge transfer and suppressing charge recombination.

### 3.2. Photocatalytic disinfection under visible light irradiation

*Salmonella*, one of the most common pathogens associated with foodborne illness in chickens, was selected to study the antibacterial ability of the prepared composites. A concentration of 0.75 mg/mL was selected as the optimum experimental concentration. The bactericidal efficiency was assessed by mixing the suspension of *Salmonella* and the prepared photocatalysts under irradiation with different time intervals (0, 5, 10, 20, 30 min). As illustrated in Fig. 3a, the bactericidal efficiency of AgVO<sub>3</sub> QDs/g-C<sub>3</sub>N<sub>4</sub> for *Salmonella* was compared to the activities of BiVO<sub>4</sub>/g-C<sub>3</sub>N<sub>4</sub> and g-C<sub>3</sub>N<sub>4</sub>. Obviously, neglected

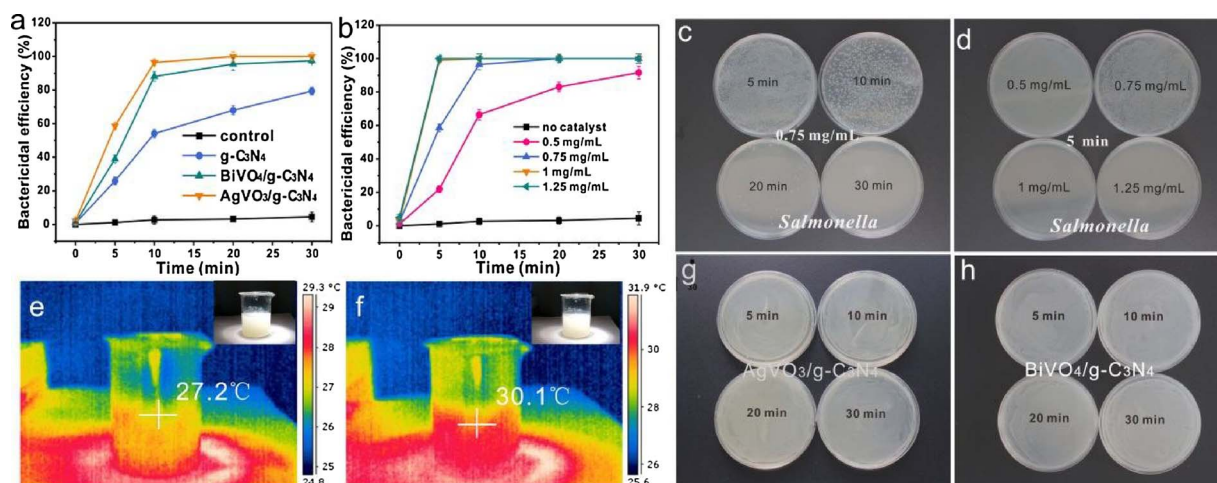


**Fig. 3.** (a) Bactericidal efficiency against *Salmonella* with different samples under concentration of 0.75 mg/mL. (b) Bactericidal efficiency against *Salmonella* with AgVO<sub>3</sub>/g-C<sub>3</sub>N<sub>4</sub> under different concentrations. (c) Bacterial colony growth in the presence of AgVO<sub>3</sub>/g-C<sub>3</sub>N<sub>4</sub> with *Salmonella*. (d) Bacterial colony growth in the presence of AgVO<sub>3</sub>/g-C<sub>3</sub>N<sub>4</sub> with *Salmonella* under different concentrations. The corresponding thermal images of AgVO<sub>3</sub>/g-C<sub>3</sub>N<sub>4</sub> at (e) 5 min and (f) 30 min irradiation. Bacterial colony growth with (g) AgVO<sub>3</sub>/g-C<sub>3</sub>N<sub>4</sub> and (h) BiVO<sub>4</sub>/g-C<sub>3</sub>N<sub>4</sub> in the dark.

antimicrobial activity was observed in blank control, indicating that illumination for sterilization doesn't work in the absence of photocatalysts. On account of the photocatalytic activity of g-C<sub>3</sub>N<sub>4</sub> under visible-light, only 54.13% inactivation of *Salmonella* was found with g-C<sub>3</sub>N<sub>4</sub> sample after 10 min. In stark contrast, with loaded vanadate QDs, significantly enhancements in bactericidal efficiency were observed on the AgVO<sub>3</sub>/g-C<sub>3</sub>N<sub>4</sub> and BiVO<sub>4</sub>/g-C<sub>3</sub>N<sub>4</sub> upon visible-light illumination. Among all of the materials, AgVO<sub>3</sub>/g-C<sub>3</sub>N<sub>4</sub> exhibited the best disinfection performance at each time interval, and the bactericidal efficiency could reach 96.4% only after 10 min visible-light irradiation, which manifests its best bactericidal ability. Furthermore, we tested the activity of pure AgVO<sub>3</sub> QDs (Fig. S5a) with and without visible light irradiation, and compared with that of the as-prepared AgVO<sub>3</sub>/g-C<sub>3</sub>N<sub>4</sub> composites to verify the photocatalytic disinfection activity. As shown in Fig. S5b, neglected antimicrobial activity was observed in dark control, indicating that AgVO<sub>3</sub> QDs are almost non-toxic to bacteria cells. And compared with the pure AgVO<sub>3</sub> QDs, the AgVO<sub>3</sub>/g-C<sub>3</sub>N<sub>4</sub> composites exhibited superior photocatalytic activity under visible light. This was caused by the superior charge separation efficiency between AgVO<sub>3</sub> QDs and g-C<sub>3</sub>N<sub>4</sub> nanostructures. In addition, we provided many previous VLD photocatalytic bacterial inactivation studies and compared the photocatalytic disinfection performances of those photocatalysts in Table S1. It was observed that our composites exhibited a superior photocatalytic disinfection compared to the most studied photocatalysts. As shown in Table S1, 7 log inactivation of *Salmonella* was obtained after treating samples for 10 min with 750 µg/mL AgVO<sub>3</sub>/g-C<sub>3</sub>N<sub>4</sub>, which was approximately 18 times faster than that of nano-TiO<sub>2</sub> (180 min). Comparing with natural magnetic sphalerite, AgVO<sub>3</sub>/g-C<sub>3</sub>N<sub>4</sub> could kill 7 log of *Salmonella* in 10 min while natural magnetic sphalerite need 360 min for inactivating 6 log of *E. coli*. Those results clearly indicated that the synthesized vanadate QDs/g-C<sub>3</sub>N<sub>4</sub> exhibited a faster photocatalytic disinfection.

The effect of the concentration of AgVO<sub>3</sub>/g-C<sub>3</sub>N<sub>4</sub> on the speed of photocatalytic disinfection was investigated by adding different quantities of AgVO<sub>3</sub>/g-C<sub>3</sub>N<sub>4</sub> to *Salmonella* aqueous solutions. According to the results in Fig. 3b, photocatalytic disinfection occurred only after the addition of AgVO<sub>3</sub>/g-C<sub>3</sub>N<sub>4</sub> composites, and the bactericidal efficiency increased with increasing photocatalyst concentration. For instance, only 22.12% of *Salmonella* were killed after 5 min when the AgVO<sub>3</sub>/g-C<sub>3</sub>N<sub>4</sub> composites suspended concentration was 0.5 mg/mL, but 58.62% of the *Salmonella* could be killed in 5 min when the photocatalyst concentration reached 0.75 mg/mL. In order to make the experimental results more clear, Fig. 3c displays the number of bacterial colonies

grown in the presence of AgVO<sub>3</sub>/g-C<sub>3</sub>N<sub>4</sub> against *Salmonella* at interval irradiation times (5, 10, 20, 30 min) on agar plates. As the images exhibited, when catalysts were added, bacteria can be killed gradually with the growth of illumination time. It can be seen that more than half of *Salmonella* were killed when the system was irradiated with visible light for 10 min. And all of the *Salmonella* were killed upon 30 min irradiation. Fig. 3d shows the bactericidal efficiency with different concentration of AgVO<sub>3</sub>/g-C<sub>3</sub>N<sub>4</sub> for 5 min visible light irradiation. Obviously, the bactericidal efficiency increased with the increasing concentration of photocatalysts. In addition, the disinfection experiments were performed at room temperature as the temperature is vital for bacterial survival under light illumination. The temperature changes were measured by a thermal imager. As shown in Fig. 3e–f, the temperature at 5 min irradiation is 27.2 °C and 30 min irradiation is 30.1 °C, only 2.9 °C increased during the experiment. At the same time, dark control experiments were conducted to test whether the photocatalyst can inactivate the cells in dark. As shown in Fig. 3g–h, the bacteria grew well on LB plates, indicating that photocatalysts could not kill the bacteria cells in dark. The results above indicated that AgVO<sub>3</sub>/g-C<sub>3</sub>N<sub>4</sub> nanosheets possess the best visible-light-driven photocatalytic disinfection performance.

### 3.3. Scavenger experiment for radical generation

Scavenger experiment is a useful way to determine bactericidal contribution for each reactive oxygen species (ROS). The h<sup>+</sup>, e<sup>-</sup>, ·OH, ·O<sub>2</sub><sup>-</sup> and H<sub>2</sub>O<sub>2</sub> were often supposed to be the reactive species for photocatalytic disinfection. However, which of them play the major role in the photocatalytic process was still unclear. Therefore, various scavengers for disinfection were employed to investigate the exact roles of these reactive oxidative species. In this study, scavengers were sodium oxalate (1 mM) for hole (h<sup>+</sup>), silver nitrate (1 mM) for electron (e<sup>-</sup>) isopropanol (1 mM) for ·OH, TEMPOL (1 mM) for ·O<sub>2</sub><sup>-</sup> and Fe (II)-EDTA (0.5 mM) for H<sub>2</sub>O<sub>2</sub>. Before conducting the experiment, we optimized the concentration of each scavenger to ensure the maximum scavenging effect but did not cause any inactivation to the bacteria. As presented in Fig. 4, in the presence of isopropanol and sodium oxalate, there were negligible changes in disinfection efficiency, indicating that ·OH and h<sup>+</sup> were not the crucial reactive species in this inactivation process. However, a significant inhibition effect of bacterial inactivation was observed after the addition of silver nitrate, which proved that the photoinduced electron (e<sup>-</sup>) was the most important role in photocatalytic process. Furthermore, considering the fact that electron can

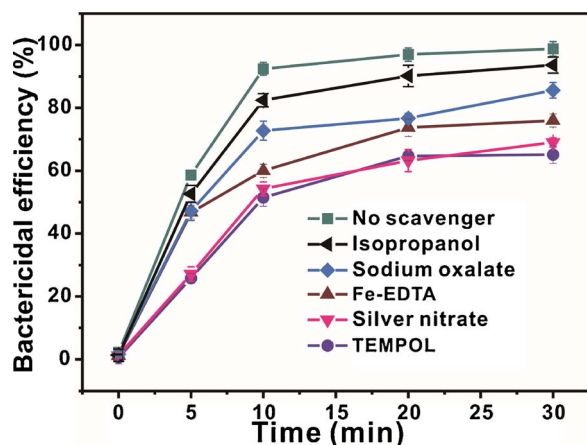


Fig. 4. Photocatalytic disinfection efficiency against *Salmonella* ( $10^7$  CFU/mL) with different scavengers.

be captured by  $O_2$  to produce other reactive oxygen species, it is essential to explore the role of these species in *Salmonella* inactivation. As shown in Fig. 4, after the addition of Fe(II)-EDTA and TEMPOL, some inhibitions to the bactericidal efficiency of  $AgVO_3/g-C_3N_4$  were noted, especially when TEMPOL was added, it was confirmed that the determined  $\cdot O_2^-$  was primary ROS accounting for photocatalytic disinfection process. The  $e^-$  can directly attack the bacterial cells and possibly be converted into other reactive substances, such as  $\cdot O_2^-$  and  $H_2O_2$ , to further oxidize the membrane of the bacterial cells. This is in agreement with previously published reports [7,13,42].

#### 3.4. Integrity of bacterial cell membranes based on fluorescence

In order to further confirm the photocatalytic disinfection effect of the  $AgVO_3/g-C_3N_4$  toward *Salmonella*, the fluorescent-based cell live/dead tests of bacterial cells were subsequently measured to verify the integrity of bacterial cell membranes, as shown in Fig. 5. The cells were stained with the fluorescent nucleic acid dyes named FITC and PI. FITC is a cell-permeable stain with green-fluorescent that could label both

live and dead cells, whereas PI is a cell-impermeable stain with red fluorescent that could label only dead cells. As shown in Fig. 5a–b, there were only a small amount of dead cells in the blank control experiments, indicating that the bacteria could survive without photocatalysts under irradiation. In stark contrast, after irradiation treatment with  $AgVO_3/g-C_3N_4$  photocatalysts, the bacterial cells exhibited a stronger red fluorescence than in the blank control, suggesting that cell membranes of *Salmonella* were damaged and labeled with red fluorescent by PI (Fig. 5c–d). The significant difference between various photocatalytic treatments demonstrates that  $AgVO_3/g-C_3N_4$  possessed an excellent photocatalytic disinfection performance via attacking the cell membranes of *Salmonella*.

#### 3.5. Membrane potential

The damaged membrane motivated us to investigate the membrane potential of *Salmonella*. The change of the membrane potential was investigated by using a membrane potential sensitive fluorochrome, DiBAC<sub>4</sub>(3) [43]. DiBAC<sub>4</sub>(3) is a class of potentially sensitive probes that can respond to depolarizing cells and bind to intracellular proteins or membranes to produce enhanced fluorescence. The increased depolarization results in additional inflow of anionic dyes and increased fluorescence. In contrast, hyperpolarization is manifested as a decrease in fluorescence. As shown in Fig. 6, bacteria treated with vanadate QDs/ $g-C_3N_4$  displayed cell membrane hyperpolarization under visible-light-driven irradiation, as evidenced by a noticeable decrease in relative fluorescence unite. In addition, more decrease in membrane potential was observed with increased time irradiation, indicating that vanadate QDs/ $g-C_3N_4$  have a good performance on photocatalytic sterilization. The reason cause hyperpolarization could be that ROS directly attack the bacteria cell membrane making the positively charged ions from the cytoplasm into the cell exterior. The results manifest that ROS could act on cell membrane, causing cell hyperpolarization [44].

#### 3.6. Bacterial decomposition and biomolecule leakage of bacteria

In order to understand the damage process of bacterial cells in

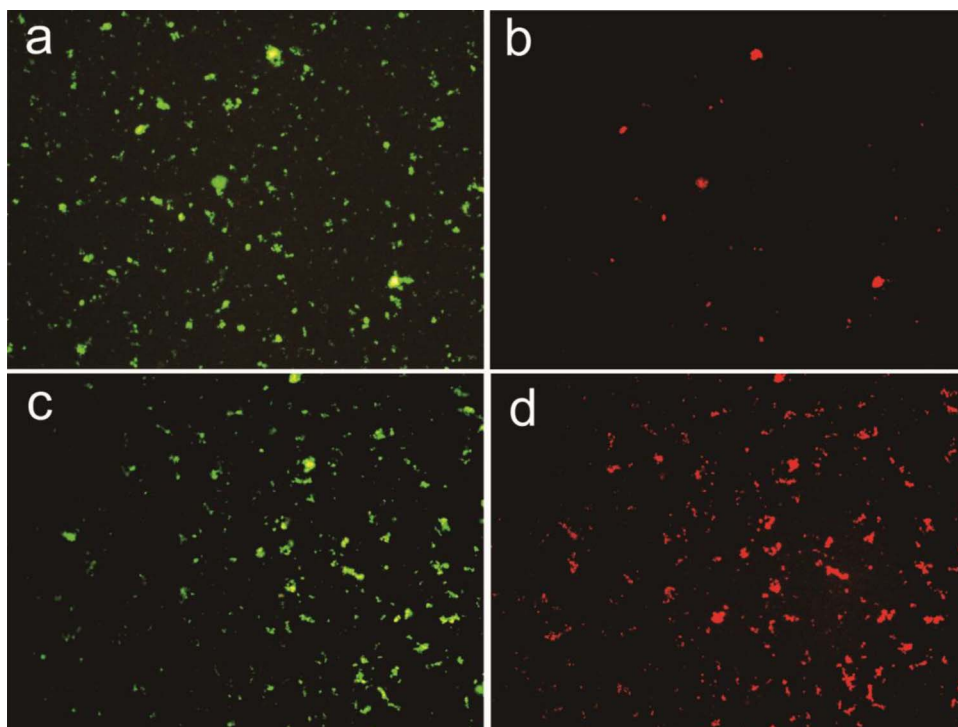


Fig. 5. Fluorescent images of live and dead *Salmonella*: (a–b) Treatment without photocatalysts under irradiation at 30 min; (b–c) Treatment with  $AgVO_3/g-C_3N_4$  photocatalysts under irradiation at 30 min.

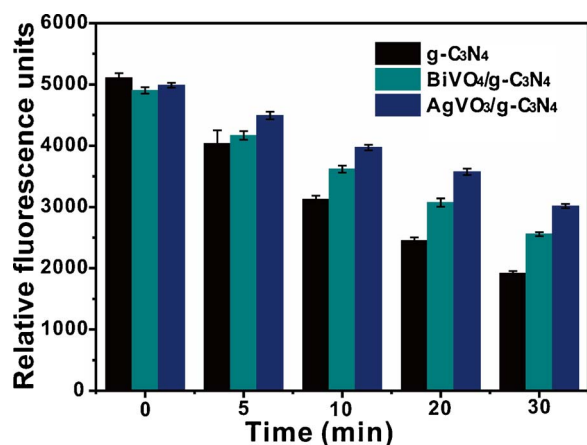


Fig. 6. Effects of vanadate QDs/g-C<sub>3</sub>N<sub>4</sub> on the membrane potentials toward *Salmonella*.

vanadate QDs/g-C<sub>3</sub>N<sub>4</sub> films under visible light, SEM technology (Fig. 7) was utilized to detecting the structure and morphological changes of *Salmonella* at different time intervals. Fig. 7a showed the SEM image of *Salmonella* before photocatalytic sterilization, where a well-preserved cell wall could be observed and homogeneous coloring inside. The flagellum of *Salmonella* is obviously intact. After 5 min irradiation contacting with AgVO<sub>3</sub> QDs/g-C<sub>3</sub>N<sub>4</sub>, the bacteria cells were attached to the materials and cell membrane start to wrinkle (Fig. 7b). After 10 min of treatment, the cell membrane shrinkage becomes more serious (Fig. 7c). By 20 min, the cell wall became deformed with some small

pits and salient points, demonstrating that some active substances, such as  $e^-$  and  $\cdot O_2^-$  had been rapidly produced and acted on the bacterial surface in the photocatalytic disinfection process (Fig. 7d). At the end of the irradiation (Fig. 7e–f), almost the entire cell surface was occupied by pores, indicating that the bacterial cells in the materials were completely distorted. Undoubtedly, the *Salmonella* cells were completely killed by AgVO<sub>3</sub> QDs/g-C<sub>3</sub>N<sub>4</sub> composites under visible light irradiation.

The damage of the cell membrane inspired us to investigate the bacterial contents, such as 16SrDNA and total protein, in which we could detect during the disinfection process (Fig. 7g–i). As shown in Fig. 7g, obviously, there were no amplification products of 16SrDNA in the negative control (lane 1), and almost nothing were amplified in the treatments of *Salmonella* without photocatalysts under illumination (lanes 2, 4, 6, 8) compared with positive control (lane 10), proving that light is useless without photocatalysts. In contrast, the leakages of 16SrDNA were more obvious at different time intervals (lanes 3, 5, 7, 9). In addition, the total protein was increased with extended irradiation time, which matched well with bactericidal efficiency (Fig. 7i). The above results indicated that the ROS which produced by AgVO<sub>3</sub> QDs/g-C<sub>3</sub>N<sub>4</sub> under visible light irradiation attacked the bacteria cells, and released the 16SrDNA and total protein. Therefore, it could be concluded that the integrity of the bacterial cells was not compromised without photocatalysts, whereas it was seriously destroyed after photocatalytic disinfection. Furthermore, experiments on *S. aureus* were selected to investigate the antibacterial ability for Gram-positive bacteria. As shown in Fig. 7h and Fig. S6, the quantities of leaked 16SrDNA and total protein in *S. aureus* were enhanced with increasing irradiation

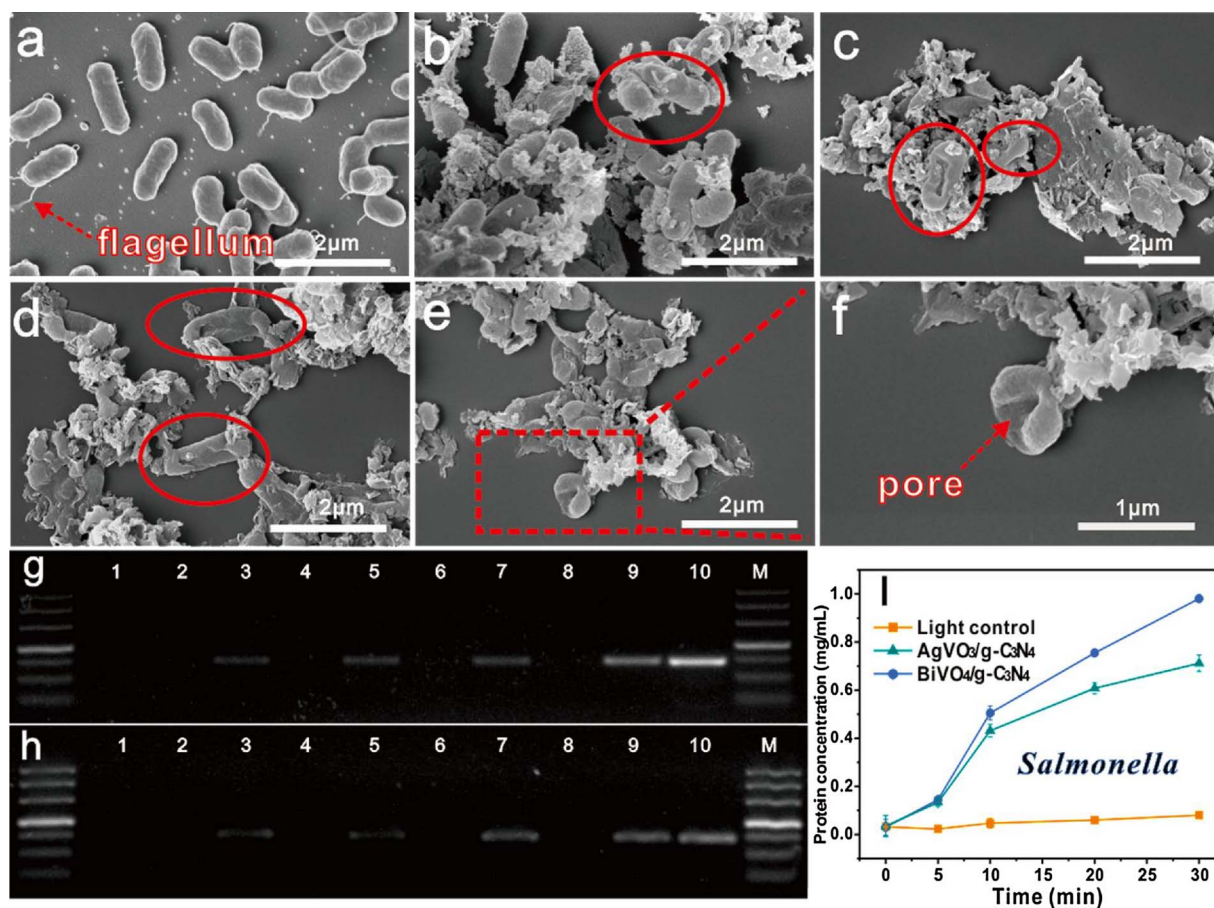


Fig. 7. SEM images of *Salmonella* ( $10^7$  CFU/mL) treated with AgVO<sub>3</sub>/g-C<sub>3</sub>N<sub>4</sub> (0.75 mg/mL) under irradiation for (a) 0, (b) 5, (c) 10, (d) 20, (e) 30, (f) 60 min (magnified SEM image). (g) PCR for *Salmonella*. (h) PCR for *S. aureus* (Lane 1: negative control; lanes 2, 4, 6, and 8: the treatments without photocatalysts under irradiation at time intervals of 5, 10, 20, 30 min, respectively; lanes 3, 5, 7, and 9: the treatments with photocatalysts under light irradiation at time intervals of 5, 10, 20, 30 min, respectively; lane 10: positive control; DNA marker (50, 100, 150, 200, 250, 300, 350, 400, 500 bp). (i) The total protein of *Salmonella* at time interval 0, 5, 10, 20, 30 min.

time, indicating that ROS can attack both Gram-negative bacteria and Gram-positive bacteria. Moreover, the bactericidal efficiency for *Salmonella* was found to be much more effective as compared to *S. aureus* in the same condition, demonstrating that Gram-positive bacteria are more resistant to photocatalytic sterilization than Gram-negative bacteria (Fig. S7). The comparison between inactivation of Gram-positive and Gram-negative are based on the complexity and density of the bacteria cells as a whole. In our experiments, the bacterial colony growth with two representative bacteria revealed that *S. aureus* 29213 is more resistant than *Salmonella* H9812 towards visible-light-driven photocatalytic inactivation. The reasons for the different bactericidal efficiencies are usually attributed to the differences in cell wall structure between two representative bacteria. The Gram-positive bacteria have a thick mesh-like cell wall made of peptidoglycan than Gram-negative bacteria, which are expected to have an advantage in photocatalytic attack. The result well agrees with those of previous reports [45–48].

### 3.7. Mechanism for the highly improved photocatalytic disinfection of vanadate QDs/g-C<sub>3</sub>N<sub>4</sub>

To get insight into the catalytic mechanism of materials, the UV–vis diffuse reflectance spectra (UV–vis DRS) and photoluminescence (PL) spectra were conducted to study the optical properties of vanadate QDs/g-C<sub>3</sub>N<sub>4</sub>. As evidenced by UV/Vis absorption curves and Kubelka–Munk plots (Fig. 8a), the bandgap of g-C<sub>3</sub>N<sub>4</sub> is about 2.68 eV. For AgVO<sub>3</sub>/g-C<sub>3</sub>N<sub>4</sub>, the bandgap is about 2.43 eV. It is obvious that AgVO<sub>3</sub>/g-C<sub>3</sub>N<sub>4</sub> exhibit significantly increased light absorption properties and absorbance edges in comparison with g-C<sub>3</sub>N<sub>4</sub>. This result might

be due to the heterojunction formed between AgVO<sub>3</sub> QDs and g-C<sub>3</sub>N<sub>4</sub>, which enhances visible light absorption of photocatalysts. Pure AgVO<sub>3</sub> QDs and BiVO<sub>4</sub>/g-C<sub>3</sub>N<sub>4</sub> also exhibit a substantial absorption capacity in the visible-light region (Fig. S8). The bandgap of pure AgVO<sub>3</sub> QDs and BiVO<sub>4</sub>/g-C<sub>3</sub>N<sub>4</sub> are 2.45 eV and 2.54 eV, respectively. The enhanced absorption of the photocatalysts could use the utmost of visible light and subsequently produce more free electron and holes, resulting in enhancing photocatalytic disinfection. Fig. 8b shows the PL spectra of g-C<sub>3</sub>N<sub>4</sub> and AgVO<sub>3</sub>/g-C<sub>3</sub>N<sub>4</sub> under 350 nm excitation. It was observed that the emission peak intensity of the AgVO<sub>3</sub>/g-C<sub>3</sub>N<sub>4</sub> photocatalysts was significantly decreased in comparison with g-C<sub>3</sub>N<sub>4</sub>. BiVO<sub>4</sub>/g-C<sub>3</sub>N<sub>4</sub> exhibited the same situation (Fig. S9). These results suggested that the incorporation of vanadate QDs can effectively prevent the recombination of electron-hole pairs, which could guarantee its high photocatalytic disinfection.

To further evaluate the separation of the photogenerated electron-hole pairs, chemical impedance spectroscopy (EIS) was employed (Fig. 8c). Generally, the smaller arc size reflects smaller charge transfer resistance on the electrode surface. Obviously, AgVO<sub>3</sub>/g-C<sub>3</sub>N<sub>4</sub> was the smallest one, which proved an effective charge-transfer property of the photocatalyst. Photocurrent responses were also employed to estimate the separation of the photogenerated electron-hole pairs. As displayed in Fig. 8d, the photocurrent intensity increased when the light was on and rapidly decreased once the light was turned off. And the photocurrent of the AgVO<sub>3</sub>/g-C<sub>3</sub>N<sub>4</sub> is approximately 2.1 times as high as that of pure g-C<sub>3</sub>N<sub>4</sub>. BiVO<sub>4</sub>/g-C<sub>3</sub>N<sub>4</sub> also exhibited a much higher photocurrent response than g-C<sub>3</sub>N<sub>4</sub>. The enhanced photocurrent of vanadate QDs/g-C<sub>3</sub>N<sub>4</sub> indicates the effective separation of photogenerated electron-hole pairs, which matched well its rapid photocatalytic

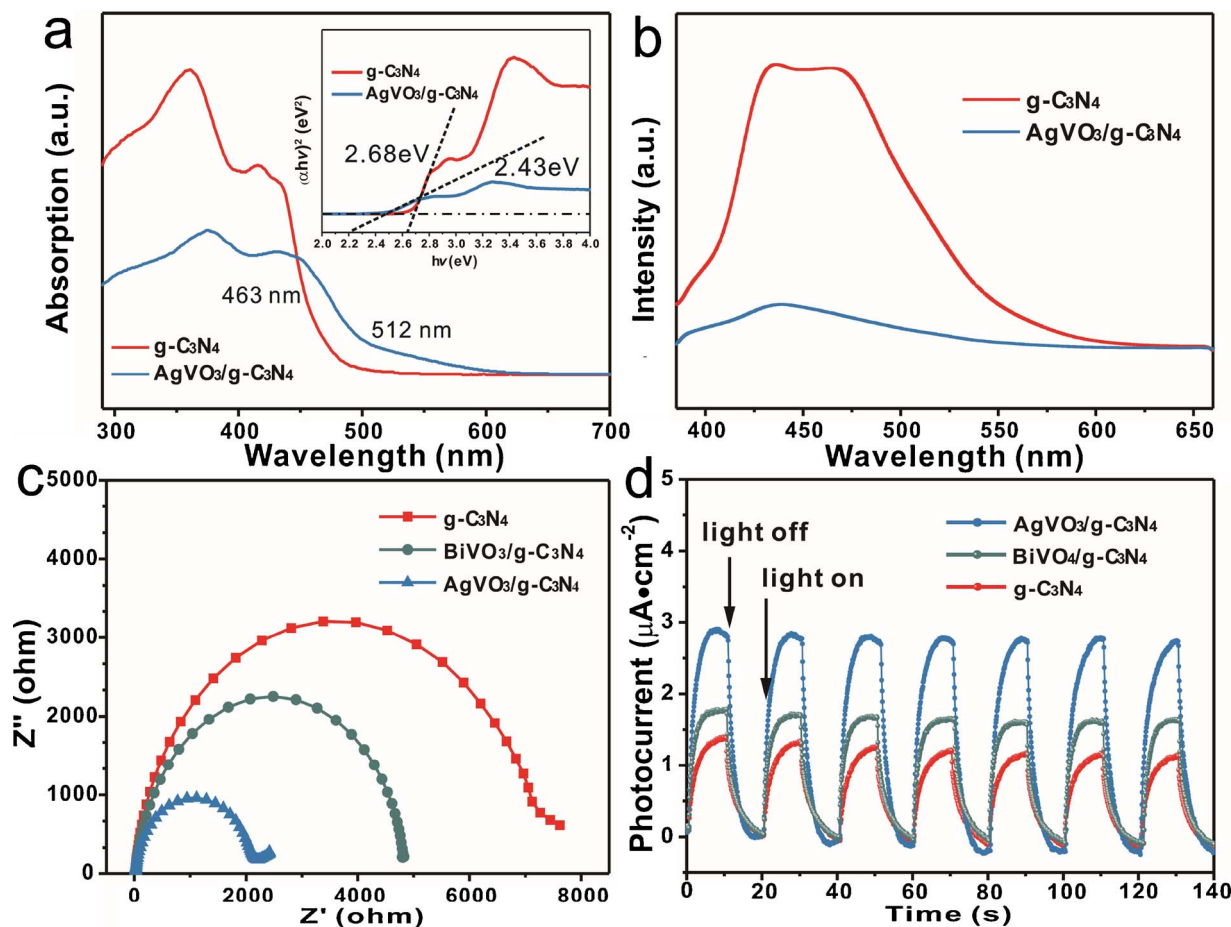


Fig. 8. (a) UV/Vis absorption and inset plots of  $(\alpha h\nu)^2$  versus photon energy for calculation of bandgap energies of g-C<sub>3</sub>N<sub>4</sub> and AgVO<sub>3</sub>/g-C<sub>3</sub>N<sub>4</sub>. (b) PL spectra of g-C<sub>3</sub>N<sub>4</sub> and AgVO<sub>3</sub>/g-C<sub>3</sub>N<sub>4</sub> at the excitation wavelength of 350 nm. (c) EIS of g-C<sub>3</sub>N<sub>4</sub>, BiVO<sub>4</sub>/g-C<sub>3</sub>N<sub>4</sub> and AgVO<sub>3</sub>/g-C<sub>3</sub>N<sub>4</sub>. (d) Photocurrent responses of g-C<sub>3</sub>N<sub>4</sub>, BiVO<sub>4</sub>/g-C<sub>3</sub>N<sub>4</sub> and AgVO<sub>3</sub>/g-C<sub>3</sub>N<sub>4</sub>.

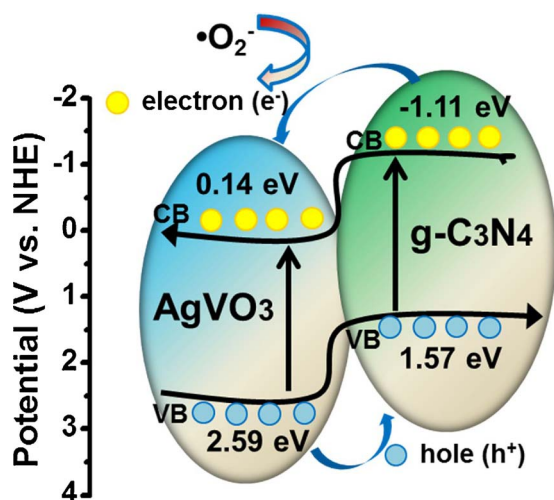


Fig. 9. Band structure and charge transfer of  $\text{AgVO}_3/\text{g-C}_3\text{N}_4$ .

disinfection.

All these parameters demonstrate that the strong interaction between  $\text{AgVO}_3$  QDs and  $\text{g-C}_3\text{N}_4$  can significantly improve the separation efficiency of photoexcited charges through better interfacial charge transfer. A diagram (Fig. 9) shows the separation of electron-hole pairs and transportation pathway between  $\text{AgVO}_3$  QDs and  $\text{g-C}_3\text{N}_4$ . The band structure of semiconductors can be estimated by applying the Mulliken electronegativity theory (Table S2) [49–51]. As presented in Fig. 9, the photoinduced electron ( $e^-$ ) is transferred from of  $\text{g-C}_3\text{N}_4$  to  $\text{AgVO}_3$  QDs because the conduction band (CB) potential of  $\text{g-C}_3\text{N}_4$  (ca.  $-1.11$  eV) is more negative than that of  $\text{AgVO}_3$  QDs (ca.  $0.14$  eV). However, the holes ( $h^+$ ) of  $\text{AgVO}_3$  (ca.  $2.59$  eV) will be transferred to the valence band (VB) of the  $\text{g-C}_3\text{N}_4$  (ca.  $1.57$  eV) because of the large potential difference between  $\text{AgVO}_3$  and  $\text{g-C}_3\text{N}_4$ . This transference could effectively enhance the separation rate of electron-hole pairs and suppress the recombination of electron-hole pairs, which lead to abundant active substances in enhancing the photocatalytic disinfection.

Based on the above research, we concluded that mechanism for the highly improved photocatalytic disinfection of vanadate QDs/ $\text{g-C}_3\text{N}_4$  comes as a result of effective separation of photoexcited charges through better interfacial charge transfer, which could promote the photocatalytic disinfection by abundant generation of ROS. The efficient separation of photogenerated electron-hole pairs enabled the vanadate QDs/ $\text{g-C}_3\text{N}_4$  to generate ROS successfully for bacteria inactivation and exhibited rapid photocatalytic disinfection. The active substances are considered to be the main oxidant that contributes to microbial cell mineralization. Especially photoinduced electron, the major role in this photocatalytic system, which could not only attack the bacterial cells but also possibly be converted into other reactive oxygen species, such as  $\cdot\text{O}_2^-$  and  $\text{H}_2\text{O}_2$ , to further oxidize the membrane of the bacterial cells. It was found that the ROS first attacked the bacterial cells membrane, making the cell membrane become deformed, and then disrupted the cell metabolism through bacterial contents, and ultimately killed all of the bacteria [45,52].

### 3.8. Cycling runs of $\text{AgVO}_3$ QDs/ $\text{g-C}_3\text{N}_4$

To study the photocatalytic stability of the prepared  $\text{AgVO}_3$  QDs/ $\text{g-C}_3\text{N}_4$  photocatalysts, four repetitive reaction processes for the photocatalytic disinfection of *Salmonella* have been conducted. The photocatalysts were recycled through a  $2\ \mu\text{m}$  luer syringe filter paper and dried in a vacuum oven before reuse [53]. As the results disclosed in Fig. 10,  $\text{AgVO}_3$  QDs/ $\text{g-C}_3\text{N}_4$  retains its high inactivation even after four cycles. In the first cycle, the efficiency of disinfection was 97.78%, slightly lesser than that of raw materials. Even after the fourth cycle,

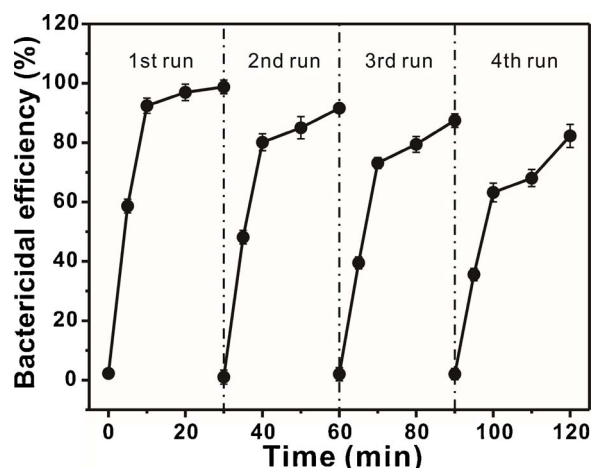


Fig. 10. Cycling runs for photocatalytic disinfection of *Salmonella*.

the bactericidal efficiency could reach 82.27%. The slight decreased disinfection efficiency was possibly due to the inevitable mass loss of materials during the recycling process. In order to explore structure stability of the photocatalyst, we made the XRD characterization of the recycled photocatalyst. The XRD patterns of  $\text{AgVO}_3/\text{g-C}_3\text{N}_4$  before and after photocatalysis show that its structure almost remains unchanged (Fig. S10). These above results revealed that  $\text{AgVO}_3$  QDs/ $\text{g-C}_3\text{N}_4$  photocatalysts can keep intact structure and photocatalytic activity after recycling several times.

## 4. Conclusion

In conclusion, we have demonstrated the efficient harvesting of visible-light for photocatalytic disinfection with a novel material, vanadate QDs/ $\text{g-C}_3\text{N}_4$ . It could be found that vanadate QDs/ $\text{g-C}_3\text{N}_4$  exhibited a faster photocatalytic disinfection compared to bare  $\text{g-C}_3\text{N}_4$  and most studied photocatalysts. The establishment of heterostructure between vanadate QDs and  $\text{g-C}_3\text{N}_4$  can lead a superior interfacial charge transfer under visible light irradiation. This enabled the  $\text{AgVO}_3$  QDs/ $\text{g-C}_3\text{N}_4$  to generate abundant ROS for bacteria inactivation in water and exhibit a rapid bactericidal efficiency of 96.4% only upon 10 min. Therefore, taking into account its easy synthetic method, chemical stability, and high photocatalytic disinfection, vanadate QDs/ $\text{g-C}_3\text{N}_4$  is an ideal photocatalyst for applications in environmental remediation.

## Acknowledgements

This research was financed by Grants from National Natural Science Foundation of China (No. 21675127), the Development Project of Qinghai Key Laboratory (No. 2017-ZJ-Y10) and the Fundamental Research Funds for the Central Universities (2014YB093, 2452015257).

## Appendix A. Supplementary data

Supplementary data associated with this article can be found, in the online version, at <https://doi.org/10.1016/j.apcatb.2017.11.060>.

## References

- [1] O.K. Dalrymple, E. Stefanakos, M.A. Trotz, D.Y. Goswami, A review of the mechanisms and modeling of photocatalytic disinfection, *Appl. Catal. B: Environ.* 98 (2010) 27–38.
- [2] L.G. Corbellini, E.d.F. Costa, M. Cardoso, M. Nauta, Quantitative microbial risk assessment of *Salmonella* in dry fermented sausage (salami) in Southern Brazil, *Microbiol. Risk Anal.* 6 (2017) 31–43.
- [3] N.J. Ashbolt, Microbial contamination of drinking water and human health from community water systems, *Curr. Environ. Health Rep.* 2 (2015) 95–106.

- [4] Y. Li, Y. Li, S. Ma, P. Wang, Q. Hou, J. Han, S. Zhan, Efficient water disinfection with Ag<sub>2</sub>WO<sub>4</sub>-doped mesoporous g-C<sub>3</sub>N<sub>4</sub> under visible light, *J. Hazard. Mater.* 338 (2017) 33–46.
- [5] M.A. Shannon, P.W. Bohn, M. Elimelech, J.G. Georgiadis, B.J. Marinas, A.M. Mayes, Science and technology for water purification in the coming decades, *Nature* 452 (2008) 301–310.
- [6] P. Wang, D. Zhang, Z. Lu, S. Sun, Fabrication of slippery lubricant-infused porous surface for inhibition of microbially influenced corrosion, *ACS Appl. Mater. Interfaces* 8 (2016) 1120–1127.
- [7] Y. Jia, S. Zhan, S. Ma, Q. Zhou, Fabrication of TiO<sub>2</sub>-Bi<sub>2</sub>WO<sub>6</sub> binanosheet for enhanced solar photocatalytic disinfection of *E. coli*: Insights on the mechanism, *ACS Appl. Mater. Interfaces* 8 (2016) 6841–6851.
- [8] S. Ma, S. Zhan, Y. Jia, Q. Shi, Q. Zhou, Enhanced disinfection application of Ag-modified g-C<sub>3</sub>N<sub>4</sub> composite under visible light, *Appl. Catal. B: Environ.* 186 (2016) 77–87.
- [9] S. Rtimi, S. Giannakis, R. Sanjines, C. Pulgarin, M. Bensimon, J. Kiwi, Insight on the photocatalytic bacterial inactivation by co-sputtered TiO<sub>2</sub>-Cu in aerobic and anaerobic conditions, *Appl. Catal. B: Environ.* 182 (2016) 277–285.
- [10] M. Agulló-Barceló, M.I. Polo-López, F. Lucena, J. Jofre, P. Fernández-Ibáñez, Solar advanced oxidation processes as disinfection tertiary treatments for real wastewater: implications for water reclamation, *Appl. Catal. B: Environ.* 136–137 (2013) 341–350.
- [11] D. Xu, W. Shi, C. Song, M. Chen, S. Yang, W. Fan, B. Chen, In-situ synthesis and enhanced photocatalytic activity of visible-light-driven plasmonic Ag/AgCl/NaTaO<sub>3</sub> nanocubes photocatalysts, *Appl. Catal. B: Environ.* 191 (2016) 228–234.
- [12] C. Liu, D. Kong, P.C. Hsu, H. Yuan, H.W. Lee, Y. Liu, H. Wang, S. Wang, K. Yan, D. Lin, P.A. Maraccini, K.M. Parker, A.B. Boehm, Y. Cui, Rapid water disinfection using vertically aligned MoS<sub>2</sub> nanofilms and visible light, *Nature Nanotech.* 11 (2016) 1098–1104.
- [13] S. Ma, S. Zhan, Y. Jia, Q. Zhou, Superior antibacterial activity of Fe<sub>3</sub>O<sub>4</sub>-TiO<sub>2</sub> nanosheets under solar light, *ACS Appl. Mater. Interfaces* 7 (2015) 21875–21883.
- [14] T. Xiong, W. Cen, Y. Zhang, F. Dong, Bridging the g-C<sub>3</sub>N<sub>4</sub> interlayers for enhanced photocatalysis, *ACS Catal.* 6 (2016) 2462–2472.
- [15] S. Fang, Y. Xia, K. Lv, Q. Li, J. Sun, M. Li, Effect of carbon-dots modification on the structure and photocatalytic activity of g-C<sub>3</sub>N<sub>4</sub>, *Appl. Catal. B: Environ.* 185 (2016) 225–232.
- [16] W.J. Ong, L.L. Tan, Y.H. Ng, S.T. Yong, S.P. Chai, Graphitic carbon nitride (g-C<sub>3</sub>N<sub>4</sub>)-based photocatalysts for artificial photosynthesis and environmental remediation: are we a step closer to achieving sustainability? *Chem. Rev.* 116 (2016) 7159–7329.
- [17] J. Oh, R.J. Yoo, S.Y. Kim, Y.J. Lee, D.W. Kim, S. Park, Oxidized carbon nitrides: water-dispersible, atomically thin carbon nitride-based nanodots and their performances as bioimaging probes, *Chem. Eur. J.* 21 (2015) 6241–6246.
- [18] G. Zhang, M. Zhang, X. Ye, X. Qiu, S. Lin, X. Wang, Iodine modified carbon nitride semiconductors as visible light photocatalysts for hydrogen evolution, *Adv. Mater.* 26 (2014) 805–809.
- [19] G. Liu, T. Wang, H. Zhang, X. Meng, D. Hao, K. Chang, P. Li, T. Kako, J. Ye, Nature-inspired environmental phosphorylation boosts photocatalytic H<sub>2</sub> production over carbon nitride nanosheets under visible-light irradiation, *Angew. Chem. Int. Ed.* 54 (2015) 13561–13565.
- [20] Z. Zhang, D. Jiang, D. Li, M. He, M. Chen, Construction of SnNb<sub>2</sub>O<sub>6</sub> nanosheet/g-C<sub>3</sub>N<sub>4</sub> nanosheet two-dimensional heterostructures with improved photocatalytic activity: synergistic effect and mechanism insight, *Appl. Catal. B: Environ.* 183 (2016) 113–123.
- [21] J. Liu, W. Li, L. Duan, X. Li, L. Ji, Z. Geng, K. Huang, L. Lu, L. Zhou, Z. Liu, W. Chen, L. Liu, S. Feng, Y. Zhang, A Graphene-like oxygenated carbon nitride material for improved cycle-life lithium/sulfur batteries, *Nano Lett.* 15 (2015) 5137–5142.
- [22] P. Yang, J. Zhao, W. Qiao, L. Li, Z. Zhu, Ammonia-induced robust photocatalytic hydrogen evolution of graphitic carbon nitride, *Nanoscale* 7 (2015) 18887–18890.
- [23] J. Xiao, Y. Xie, F. Nawaz, Y. Wang, P. Du, H. Cao, Dramatic coupling of visible light with ozone on honeycomb-like porous g-C<sub>3</sub>N<sub>4</sub> towards superior oxidation of water pollutants, *Appl. Catal. B: Environ.* 183 (2016) 417–425.
- [24] G. Dong, W. Ho, Y. Li, L. Zhang, Facile synthesis of porous graphene-like carbon nitride (C<sub>6</sub>N<sub>6</sub>H<sub>3</sub>) with excellent photocatalytic activity for NO removal, *Appl. Catal. B: Environ.* 174–175 (2015) 477–485.
- [25] Y. Zhang, J. Liu, G. Wu, W. Chen, Porous graphitic carbon nitride synthesized via direct polymerization of urea for efficient sunlight-driven photocatalytic hydrogen production, *Nanoscale* 4 (2012) 5300–5303.
- [26] G. Zhang, J. Zhang, M. Zhang, X. Wang, Polycondensation of thiourea into carbon nitride semiconductors as visible light photocatalysts, *J. Mater. Chem.* 22 (2012) 8083–8091.
- [27] K.C. Christoforidis, T. Montini, E. Bontempi, S. Zafeirotas, J.J.D. Jaén, P. Fornasiero, Synthesis and photocatalytic application of visible-light active β-Fe<sub>2</sub>O<sub>3</sub>/g-C<sub>3</sub>N<sub>4</sub> hybrid nanocomposites, *Appl. Catal. B: Environ.* 187 (2016) 171–180.
- [28] K. Li, S. Gao, Q. Wang, H. Xu, Z. Wang, B. Huang, Y. Dai, J. Lu, In-Situ-Reduced Synthesis of Ti<sup>3+</sup>-self-doped TiO<sub>2</sub>/g-C<sub>3</sub>N<sub>4</sub> heterojunctions with high photocatalytic performance under LED light irradiation, *ACS Appl. Mater. Interfaces* 7 (2015) 9023–9030.
- [29] S. Bai, X. Wang, C. Hu, M. Xie, J. Jiang, Y. Xiong, Two-dimensional g-C<sub>3</sub>N<sub>4</sub>: an ideal platform for examining facet selectivity of metal co-catalysts in photocatalysis, *Chem. Commun.* 50 (2014) 6094–6097.
- [30] N. Cheng, J. Tian, Q. Liu, C. Ge, A.H. Qusti, A.M. Asiri, A.O. Al-Youbi, X. Sun, Au-nanoparticle-loaded graphitic carbon nitride nanosheets: green photocatalytic synthesis and application toward the degradation of organic pollutants, *ACS Appl. Mater. Interfaces* 5 (2013) 6815–6819.
- [31] V.S. Rudnev, M.S. Vasilyeva, N.B. Kondrikov, L.M. Tyrina, Plasma-electrolytic formation, composition and catalytic activity of manganese oxide containing structures on titanium, *Appl. Surf. Sci.* 252 (2005) 1211–1220.
- [32] Z. Tong, D. Yang, Z. Li, Y. Nan, F. Ding, Y. Shen, Z. Jiang, Thylakoid-inspired multishell g-C<sub>3</sub>N<sub>4</sub> nanocapsules with enhanced visible-light harvesting and electron transfer properties for high-efficiency photocatalysis, *ACS Nano* 11 (2017) 1103–1112.
- [33] M. Ye, Z. Zhao, Q. Hu, L. Liu, H. Ji, Z. Shen, T. Ma, 0D/2D heterojunctions of vanadate quantum dots/graphitic carbon nitride nanosheets for enhanced visible-light-driven photocatalysis, *Angew. Chem. Int. Ed.* 56 (2017) 1–6.
- [34] J.A. Caputo, L.C. Frenette, N. Zhao, K.L. Sowers, T.D. Krauss, D.J. Weix, General and efficient C-C bond forming photoredox catalysis with semiconductor quantum dots, *J. Am. Chem. Soc.* 139 (2017) 4250–4253.
- [35] T.F. Yeh, C.Y. Teng, S.J. Chen, H. Teng, Nitrogen-doped graphene oxide quantum dots as photocatalysts for overall water-splitting under visible light illumination, *Adv. Mater.* 26 (2014) 3297–3303.
- [36] S.Y. Lim, W. Shen, Z. Gao, Carbon quantum dots and their applications, *Chem. Soc. Rev.* 44 (2015) 362–381.
- [37] J. Zhou, Y. Yang, C.Y. Zhang, Toward biocompatible semiconductor quantum dots: from biosynthesis and bioconjugation to biomedical application, *Chem. Rev.* 115 (2015) 11669–11717.
- [38] H. Yu, R. Shi, Y. Zhao, G.I. Waterhouse, L.Z. Wu, C.H. Tung, T. Zhang, Smart utilization of carbon dots in semiconductor photocatalysis, *Adv. Mater.* 28 (2016) 9454–9477.
- [39] D. Jiang, X. Du, L. Zhou, H. Li, K. Wang, New insights toward efficient charge-separation mechanism for high-performance photoelectrochemical aptasensing: enhanced charge-carrier lifetime via coupling ultrathin MoS<sub>2</sub> nanoplates with nitrogen-doped graphene quantum dots, *Anal. Chem.* 89 (2017) 4525–4531.
- [40] A. Boulesbaa, K. Wang, M. Mahjouri-Samani, M. Tian, A.A. Puretzky, I. Ivanov, C.M. Rouleau, K. Xiao, B.G. Sumpter, D.B. Geohegan, Ultrafast charge transfer and hybrid exciton formation in 2D/0D heterostructures, *J. Am. Chem. Soc.* 138 (2016) 14713–14719.
- [41] J.W. Xu, Z.D. Gao, K. Han, Y. Liu, Y.Y. Song, Synthesis of magnetically separable Ag<sub>3</sub>PO<sub>4</sub>/TiO<sub>2</sub>/Fe<sub>3</sub>O<sub>4</sub> heterostructure with enhanced photocatalytic performance under visible light for photoinactivation of bacteria, *ACS Appl. Mater. Interfaces* 6 (2014) 15122–15131.
- [42] D. Xia, W. Wang, R. Yin, Z. Jiang, T. An, G. Li, H. Zhao, P.K. Wong, Enhanced photocatalytic inactivation of *Escherichia coli* by a novel Z-scheme g-C<sub>3</sub>N<sub>4</sub>/m-Bi<sub>2</sub>O<sub>4</sub> hybrid photocatalyst under visible light: the role of reactive oxygen species, *Appl. Catal. B: Environ.* 214 (2017) 23–33.
- [43] C. Shi, Y. Sun, Z. Zheng, X. Zhang, K. Song, Z. Jia, Y. Chen, M. Yang, X. Liu, R. Dong, X. Xia, Antimicrobial activity of syringic acid against *Cronobacter sakazakii* and its effect on cell membrane, *Food Chem.* 197 (2016) 100–106.
- [44] E. Sanchez, N. Heredia, R. Camacho-Corona Mdel, S. Garcia, Isolation, characterization and mode of antimicrobial action against *Vibrio cholerae* of methyl gallate isolated from *Acacia farnesiana*, *J. Appl. Microbiol.* 115 (2013) 1307–1316.
- [45] H.A. Foster, I.B. Ditta, S. Varghese, A. Steele, Photocatalytic disinfection using titanium dioxide: spectrum and mechanism of antimicrobial activity, *Appl. Microbiol. Biotechnol.* 90 (2011) 1847–1868.
- [46] A. Pal, S.O. Pehkonen, L.E. Yu, M.B. Ray, Photocatalytic inactivation of Gram-positive and Gram-negative bacteria using fluorescent light, *J. Photochem. Photobiol. A* 186 (2007) 335–341.
- [47] K.P. Kühn, I.F. Chaberny, K. Massholder, M. Stickler, V.W. Benz, H.-G. Sonntag, L. Erdinger, Disinfection of surfaces by photocatalytic oxidation with titanium dioxide and UVA light, *Chemosphere* 53 (2003) 71–77.
- [48] J. Ren, W. Wang, S. Sun, L. Zhang, J. Chang, Enhanced photocatalytic activity of Bi<sub>2</sub>WO<sub>6</sub> loaded with Ag nanoparticles under visible light irradiation, *Appl. Catal. B: Environ.* 92 (2009) 50–55.
- [49] X. Meng, Z. Li, H. Zeng, J. Chen, Z. Zhang, MoS<sub>2</sub> quantum dots-interspersed Bi<sub>2</sub>WO<sub>6</sub> heterostructures for visible light-induced detoxification and disinfection, *Appl. Catal. B: Environ.* 210 (2017) 160–172.
- [50] R.S. Mulliken, A new electroaffinity scale; together with data on valence states and on valence ionization potentials and electron affinities, *J. Chem. Phys.* 2 (1934) 782–793.
- [51] X. Chang, T. Wang, P. Zhang, J. Zhang, A. Li, J. Gong, Enhanced surface reaction kinetics and charge separation of p-n heterojunction Co<sub>3</sub>O<sub>4</sub>/BiVO<sub>4</sub> photoanodes, *J. Am. Chem. Soc.* 137 (2015) 8356–8359.
- [52] H.M. Yadav, S.V. Otari, R.A. Bohara, S.S. Mali, S.H. Pawar, S.D. Delekar, Synthesis and visible light photocatalytic antibacterial activity of nickel-doped TiO<sub>2</sub> nanoparticles against Gram-positive and Gram-negative bacteria, *J. Photochem. Photobiol. A* 294 (2014) 130–136.
- [53] D. Xia, Z. Shen, G. Huang, W. Wang, J.C. Yu, P.K. Wong, Red Phosphorus: an earth-abundant elemental photocatalyst for Green bacterial inactivation under visible light, *Environ. Sci. Technol.* 49 (2015) 6264–6273.